

Higher order twin modes in martensitic NiTi—The $(20\bar{1})$ case

T. Ezaz^{a,*}, H. Sehitoglu^{a,*}, W. Abuzaid^a, H.J. Maier^b

^a Department of Mechanical Science and Engineering, University of Illinois at Urbana-Champaign, 1206 W. Green St., Urbana, IL 61801, USA

^b University of Paderborn, Lehrstuhl für Werkstoffkunde, D-33095 Paderborn, Germany

ARTICLE INFO

Article history:

Received 22 May 2012

Received in revised form

6 August 2012

Accepted 7 August 2012

Keywords:

Twins

Martensite (201)

NiTi shape memory

ab-initio

ABSTRACT

NiTi alloys in the martensitic phase deform by detwinning of the martensite variants succeeded by deformation twinning of the single crystal of martensite. One of the deformation twinning modes of the martensite is denoted as $(20\bar{1})[\bar{1}0\bar{2}]$. In this work, we establish how twinning on the $(20\bar{1})$ planes develops via the combination of homogeneous shear and shuffle and establish its energy barrier via atomistic simulations. We calculate the slip barrier in addition to the twin barrier ruling out the potential for plastic flow via slip in the $(20\bar{1})$ plane. The $(20\bar{1})[\bar{1}0\bar{2}]$ mode succeeds the (001) and (100) compound twinning modes which have lower energy barriers. It plays a significant role in allowing deformation to higher strains in the martensitic phase. Therefore, the insight into the $(20\bar{1})[\bar{1}0\bar{2}]$ twinning mode is important in extending the shape memory strains in NiTi alloys and towards better understanding of shape memory alloys in general.

© 2012 Elsevier B.V. All rights reserved.

1. Introduction

The transforming alloys such as NiTi can be utilized in shape memory or pseudoelasticity modes depending on the application [1]. In the case of shape memory, the material is initially deformed in the martensitic phase (B19') to achieve a single variant of martensite [2]. During subsequent deformation of the martensite, the martensite undergoes detwinning followed by mechanical (deformation) twinning. Upon heating, the martensite reverts to austenite and strain recovery occurs. In the case of pseudoelasticity the material undergoes austenite to martensite transformation, at a constant temperature [3]. Upon unloading the martensite reverts back to austenite. In both cases, at high strains, martensite undergoes deformation by twinning and we focus on the higher order twin modes in the present article.

Previous works on shape memory can be classified into three categories: the work on materials science has established the crystallography of the phase change [1,4,5] and twin/slip systems that are activated [6–8] while the work in micro-mechanics has focused on prediction of stress–strain curves (or strain–temperature curves) and their correspondence to experiments [9–14]. A third field has emerged more recently, under the general topic of ‘atomic simulations’, that determines the energy barriers, and sheds light into the atomic movements responsible for transformation [15,16] and twinning [17,18]. These simulations

have the advantage of determining precisely the fault energies and their variation with atomic displacements. Such displacements are much more complicated in low symmetry alloys compared to pure face centered cubic (fcc) metals. The atomic ‘simulations’ are either of the semi-empirical molecular dynamics type or the more rigorous first principle based density functional theory (electronic structure) calculations. For binary alloys such as NiTi molecular dynamics potentials are at an early stage of development [19,20], and DFT is preferred. Therefore, the present work employed electronic structure calculations for understanding deformation twinning at high strains in NiTi. NiTi is an alloy with remarkable properties. Some of its unusual properties stem from its high resistance to slip while permitting transformation and twinning at lower stress magnitudes. It is through atomistic simulations that this resistance can be quantified.

To gain a better understanding of the twinning in NiTi it is instructive to study the schematic shown in Fig. 1. We address the atomistic mechanism of twin formation and growth in terms of energy barriers, i.e. GPFE (Generalized Plane Fault Energy), and for the slip mode via GSFE (Generalized Stacking Fault Energy). In the electronic structure calculations [18], the GPFE characterizes twin formation (Fig. 1(a) and (c)) while the GSFE is an indicator of slip resistance (Fig. 1(d)). In GPFE, the atoms are displaced by the twin Burgers vector magnitude one layer at a time building a twin embryo. Therefore, the total displacement increases linearly with distance from the twin boundary. In GSFE calculations, the atoms are displaced by the Burgers vector magnitude above the slip plane. Therefore, the displacement is uniform in the upper part of the crystal.

In Fig. 1(a) a reflective twin is generated by the passage of partial dislocations layer by layer. This is also typically observed

* Corresponding authors. Tel.: +1 510 604 7872, +1 217 333 4112; fax: +1 217 244 6534.

E-mail addresses: tezaz@illinois.edu (T. Ezaz), huseyin@illinois.edu (H. Sehitoglu).

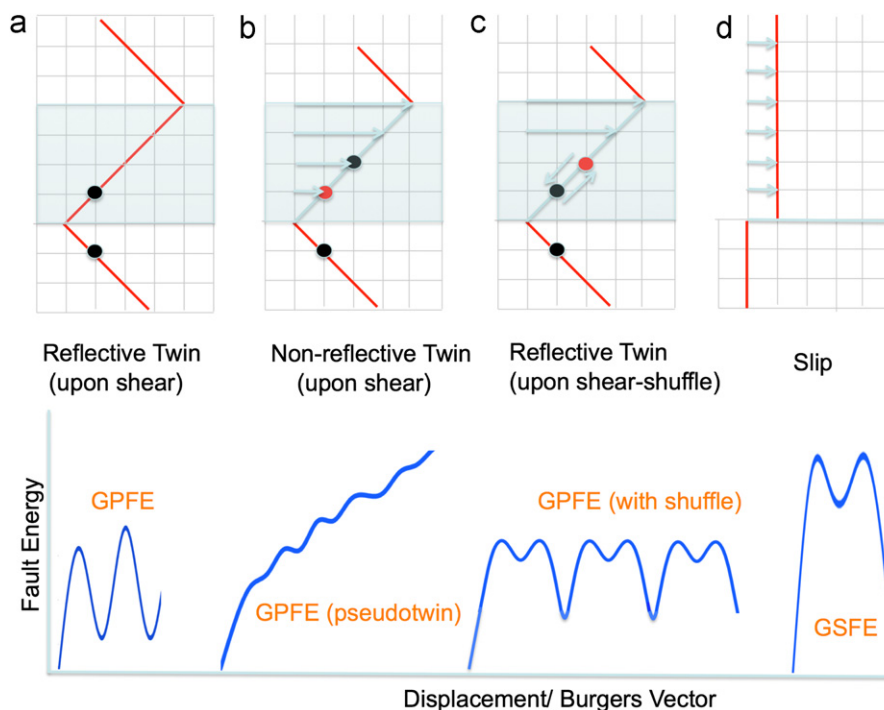


Fig. 1. The GPFE and GSFE construction relevant to twinning and slip in metals outlining the different scenarios that can occur in NiTi martensites.

in fcc metals as well as in the (001) twinning in the B19' case. The first peak in the GPFE curve could be different than the second but the curves stabilize after three layers in most cases. For the (100) B19' and (112) B2 (austenite) and (114) B2 cases, the application of shear on successive layers does not result in a reflective twin as shown in Fig. 1(b). In fact it does generate an alloy structure where the atomic sites are at a twinned position, however, the ordering of atoms is different from the original structure. This twinned structure is usually termed as "pseudo-twin". In case of the pseudo-twin, the fault energy curve does not stabilize with shear on subsequent layers and the energy grows as the twin increases in width, therefore the formation of pseudo-twins is unlikely. In the third case, denoted in Fig. 1(c), shuffling of the atoms occurs resulting in a reflective twin. We refer to this case as 'GPFE with shuffle'. This occurs for the $(20\bar{1})[\bar{1}0\bar{2}]$ case as studied here, and also for the (100)[001] B19' [18] and (112) B2 case studied previously [21]. This shuffle can occur simultaneously with shear, but its exact variation is not known a priori. We note that the twin migration energies stabilize in this case as well but require more than three layers. Finally, the deformed crystal and the corresponding energy variation (GSFE) are shown in Fig. 1(d) for the case of slip. The magnitude of this energy barrier can be substantially higher for the twin barrier shown in Fig. 1(c). We note that the classification of twins into the shear and combined shear-shuffle cases as shown in Fig. 1(a) and (c) facilitates our understanding, especially for ordered shape memory alloys.

In the presence of both shear and shuffle during twin growth, one obtains a 'minimum energy path (MEP)' pointing out their exact coupling. Energy calculation along the MEP establishes the twin barrier energy, *i.e.* the GPFE (Fig. 1(c)). The MEP has an energy barrier that is considerably lower than the GSFE barrier ruling out the propensity of slip compared to twinning. The present paper elaborates on this concept in detail.

The basic crystal structure of the B19' martensite is shown in Fig. 2. The plane of interest shaded $(20\bar{1})$ is noted in this figure as well as the planes (001) and (100). The *c*-axis is the long axis and the *a*-axis is the short one, while the *b*-axis is intermediate.

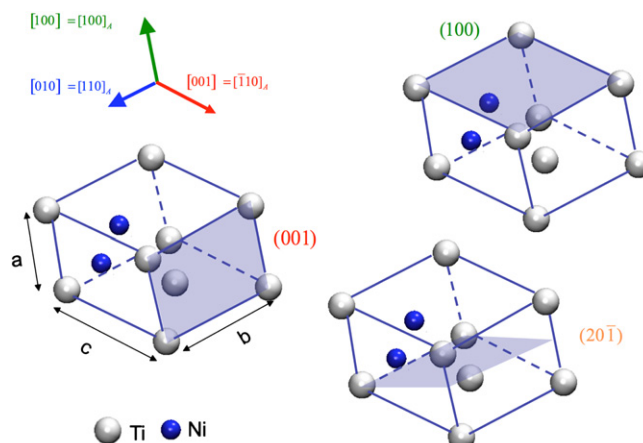


Fig. 2. Perspective projection of the B19' martensite showing the twin planes. The specific focus in this study is on the $(20\bar{1})$ plane as depicted above.

Note that the monoclinic angle between the [100] and [001] axis is 97.8° . We note that the lattice constants *a*, *b*, and *c* are calculated from energy minimization for the B19' lattice.

We consider deformation of NiTi martensite in the regime well below the martensite finish temperature. This state is achieved by cooling to below M_f (martensite finish temperature). The initial deformation of the martensitic phase occurs primarily via detwinning of the Type II-1 transformation twins as shown in the schematic in Fig. 3, followed by {001} compound twinning and the higher twin modes. In Fig. 3 the red line represents the deformation of the martensite and the blue line shows the recovery (martensite to austenite transformation upon heating). The details of deformation of the martensite are important as its behavior affects the subsequent shape memory behavior. The Type II-1 twins are predicted from the phenomenological theory of martensite, and during detwinning one variant grows in expense of other variants. The (001) twins are also observed particularly in aged NiTi or nickel rich compositions [6,22,23] and they also undergo detwinning processes. The Type II-1 twins and

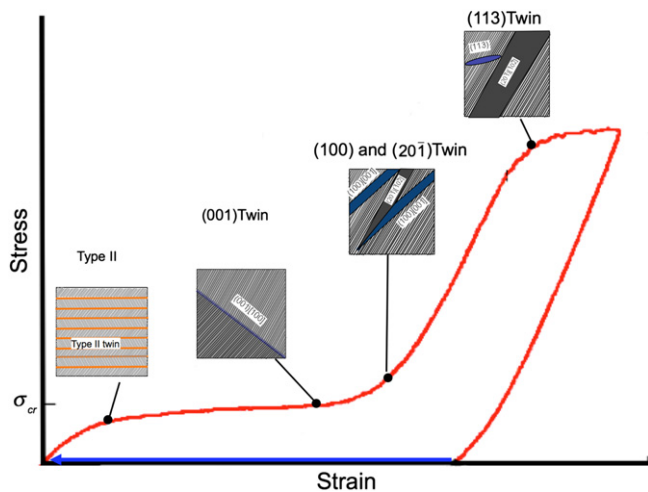


Fig. 3. The twinning mechanisms and their evolution at different stages of the stress–strain curve (adapted from Zhang et al. [7]) in NiTi.

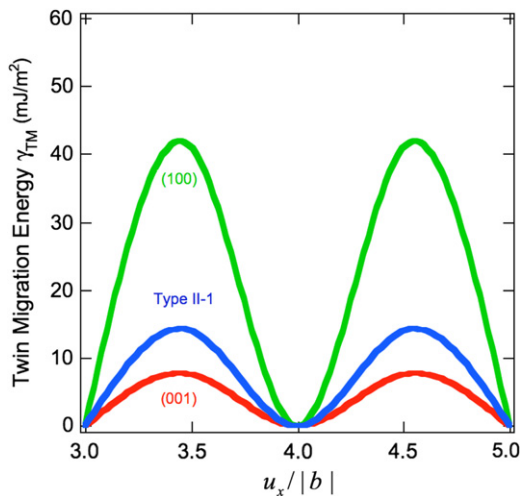


Fig. 4. Twin migration energies during twin growth of a 3 layer twin to a 5 layer twin in (001) [100] and (100)[001] and Type II-1 cases, respectively. Note that the magnitude of $|b|$ is different for all the three twin modes.

the (001) twins are operative at the early stages of the deformation. These are succeeded by deformation twinning in (100) planes and $(20\bar{1})$ planes. The $(20\bar{1})$ occurs upon deformation of the martensite at moderate strains ($> 3\%$). It occurs as deformation proceeds beyond the plateau region where the interactions of different twin systems become prevalent. At higher strains, the (113) twin system can be activated as noted in Fig. 3. At even higher strain levels, the plastic deformation via slip is possible resulting in the decrease of strain hardening.

Our previous work on Type II-1 twinning and compound twinning established their energy barriers [17,18]. The energy barriers for (100) is higher than for the (001) case. The migration energy barriers are shown in Fig. 4 (the horizontal axis in Fig. 4 is the normalized shear displacement). We note that the Type II-1 and (001) cases have clearly lower barriers compared to the (100) case. The results in Fig. 4 show why twinning can readily occur in NiTi martensites as these energy barriers are rather low ($< 15 \text{ mJ/m}^2$) for both Type II-1 and (001) cases.

The activation of the $(20\bar{1})$ system imparts additional ductility to martensite during deformation (and also during marforming). In the work of Zhang et al. [7] deformation in the range 6–12% resulted in considerable volume fraction of $(20\bar{1})$ twins, and in

Karaman et al.'s [24] work the strains exceeded 6% as well. Hence, the $(20\bar{1})$ mode is especially important in deformation processes where higher strains are required or when pseudoelastic or shape memory response over a broader strain range ($> 6\%$) is desired. Clearly, activation of higher twin modes could represent an important avenue to expand the strain range of shape memory alloys. Nevertheless, little is known about the development during deformation and will therefore be addressed in the current work.

2. Experimental results

The nearly equiatomic NiTi alloy used in this study was heat treated to render a martensitic state at room temperature. After single crystal growth, the specimens were solutionized at 1000°C for 2 h in an inert gas atmosphere. The sample in this case was a single crystal oriented in the [001] direction. The material was heat treated at 450°C for 100 h then water quenched. This heat treatment resulted in an austenite start temperature of 45°C and a martensite start of 40°C . The transformation temperatures were determined using differential scanning calorimetry (DSC) (see Fig. 5a).

The tensile experiments were conducted on small dog bone specimens at room temperature (28°C). Upon cooling below M_f and reheating to RT the specimens were in a fully martensitic state (see Fig. 5(a)). The deformation is initially elastic followed by different twin modes in the nonlinear regime. A typical stress–strain curve is shown in Fig. 5(b). We superimposed the expected twinning modes in the inset images on the stress–strain curve. We note that (001) and (100) cases are not equivalent because of different lattice constants in these respective directions. The (001) and (100) twinning modes are discussed in detail with TEM evidences in earlier work [18] and the $(20\bar{1})$ results are discussed below.

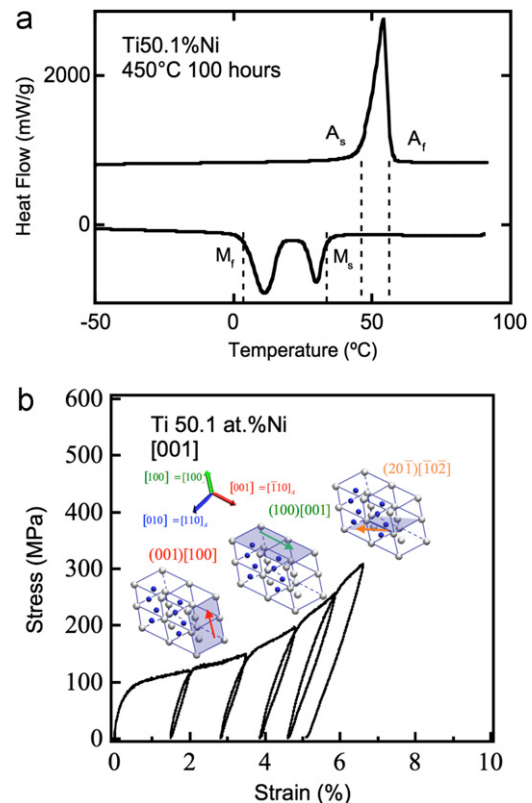


Fig. 5. (a) Differential scanning calorimetry results for the 50.1% NiTi showing martensitic structure at room temperature (achieved upon cooling below M_f and then heating to RT). (b) Stress–strain response of NiTi in the martensitic state displaying the different twinning modes as a function of applied strain.

Additional confirmation of the activation of the $(20\bar{1})$ twinning mode was obtained using Transmission Electron Microscopy (TEM) analysis. We observed the transition from the self-accommodated transformation twin structure to a deformation twinned state with $(20\bar{1})$ twins as shown in Fig. 6. Initially, the martensite morphology shows self-accommodating martensite (Fig. 6(a)) while the deformed sample reveals the presence of $(20\bar{1})$ twinning (Fig. 6(b)).

High resolution, *ex-situ* DIC measurements were performed at the end of each loading increment (such as shown in Fig. 5(b)). The DIC measurement resolution, which can be approximated by subset size, is dependent on the magnification level at which images are taken. Higher magnification leads to improved resolution. Smaller subset sizes improve the spatial resolution of the DIC fields. This is accomplished by reducing the amount of strain averaging, typically performed in correlations with larger subset sizes. The downside of increasing magnification is the reduction of field of view (*i.e.*, reduction in image size). Thus, the area that

can be monitored with one image will become small; this requires multiple images to be captured to cover the required region of interest. With reference and deformed image arrays acquired, to obtain the strain fields throughout the region of interest resulting from the applied deformation, the image arrays can be stitched together to form very large images. The details of this technique has been described in earlier work [25] and further relevant details are given in the Appendix.

Three different twin systems $\{201\}$, $\{001\}$ and $\{100\}$ are identified utilizing DIC in deformed NiTi samples and an example is shown in Fig. 7. The local strains exceed 3.5%. We note that, all the three twin systems, $(001)[100]$, $(100)[001]$ and $(20\bar{1})[\bar{1}0\bar{2}]$ have an out of plane viewing direction in $[010]$. Hence, these twin systems can be identified without any surface effect with the $[010]$ viewing direction. The angles between (001) and (100) and (100) and $(20\bar{1})$ twins are measured to be 97.8° and 18° respectively.

It is important to understand the details of the $(20\bar{1})$ mode, specifically the shear magnitude, the shuffles, and the energy

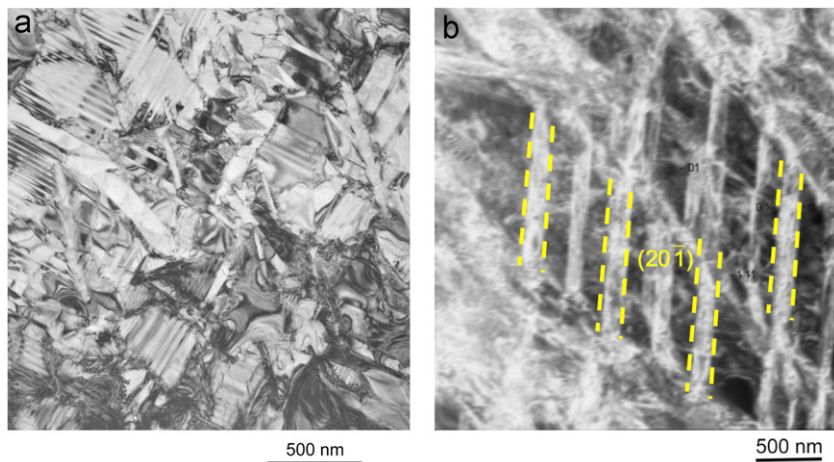


Fig. 6. TEM image of NiTi in the martensitic state, (a) the self accomodating structure, (b) after deformation showing the presence of $(20\bar{1})$ system (dashed line).

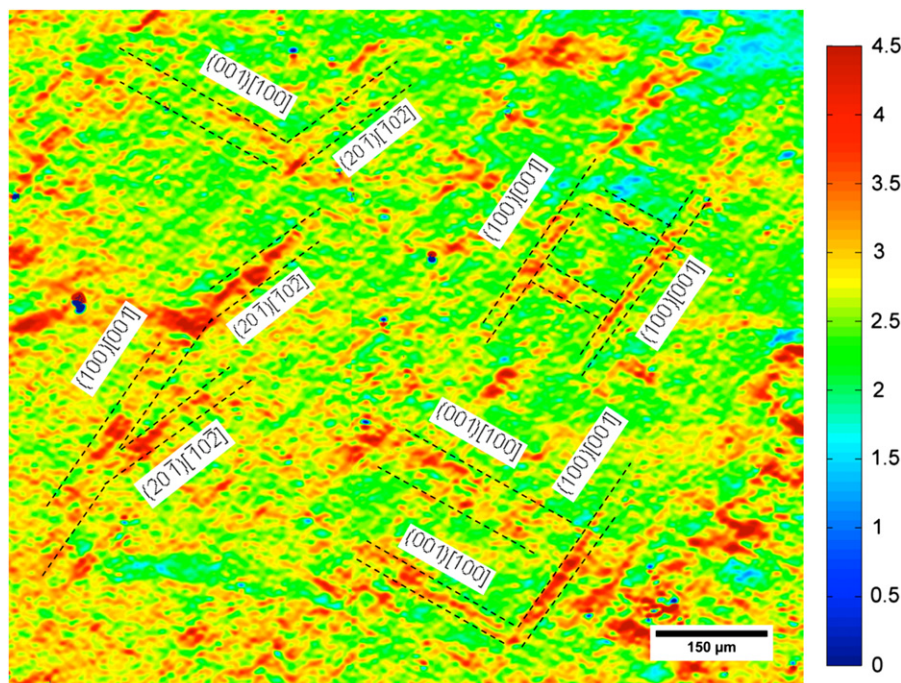


Fig. 7. The DIC image of a deformed NiTi sample showing the activation of three twin modes, $\{201\}$, $\{001\}$ and $\{100\}$. The local strains exceed 3.5%. The angles between (001) and (100) and (100) and $(20\bar{1})$ twins are measured to be 97.8° and 18° respectively.

barrier for twin migration. Despite the importance of this twinning mode, the details of the twinning mechanism have received less attention. The martensite crystallography is rather complex for a monoclinic lattice and in the presence of a monoclinic angle not 90°. The paper addresses the details of the (20 $\bar{1}$) case.

3. Simulations

We used spin-polarized, *ab-initio* calculation to properly determine the energy states of the undeformed and deformed energy states of NiTi martensite during the (20 $\bar{1}$)[$\bar{1}0\bar{2}$] twin growth. The *ab-initio* calculations were conducted via the Density functional theory based Vienna *ab-initio* Simulation Package (VASP) [26] and the generalized gradient approximation (GGA) [27] is implemented on a projection-augmented wave (PAW). PAW is an efficient all-electron method and necessary for high accuracy when transition metals such as Ti are considered. For non-uniform charge densities like NiTi, the exchange-correlation energy can deviate significantly from uniform electron gas at every point in the system. This deviation can be expressed in terms of the gradient and higher spatial derivatives of the total charge density. The GGA uses the gradient of the charge density to correct this deviation. Monkhorst-Pack 9 × 9 × 9 *k*-point meshes were used for Brillouin zone integration. All calculations were performed using an energy cut-off of 350 eV, hence all plane-waves with a kinetic energy smaller than 350 eV were included in the basis. During strain controlled shear deformation, only ion positions were relaxed and both volume and shape of the simulation box were held constant ensuring the correct monoclinic angle of martensite. Ionic relaxation was performed by a conjugate gradient algorithm which brings the ion to an instantaneous ground state. The electronic convergence threshold was set to 1 × 10⁻⁴ eV per unit cell. Ionic relaxation was stopped when absolute values of internal forces were smaller than 5 × 10⁻⁴ eV/Å. During shearing of the supercell, primitive vectors were adjusted which maintains the correct stacking between the adjacent supercells ensuring periodicity. The structural parameter of NiTi in B19' phase have been described in earlier work [18].

The transition path between local minima at the 3rd layer and 4th layer twin was obtained from the energy surface (PES) with minimum energy paths (MEP). In addition to the lowest energy path, MEP allowed us to identify the saddle point energy (TS), which acts as the peak barrier during the twin growth process. In this study, the MEP was calculated based on the well-established modified string method [28].

3.1. GPFE-(20 $\bar{1}$)[$\bar{1}0\bar{2}$] twinning

The (20 $\bar{1}$)[$\bar{1}0\bar{2}$] type twin nucleates at higher strain (> 4%), following the generation of (001) and (100) type twins. This mode is particularly important where higher strains or when pseudoelastic response over a broad strain range is desired. The required shear strain to generate a twinned structure is 0.338, a higher value compared to the required shear for (001) or (100) twins as shown in Table 1. Hence, the high ductility of the martensite is

attributable to the formation of twins in the (20 $\bar{1}$) plane. We also note that shuffle occurs in some cases but not in others (Table 1). The presence of shuffle complicates the calculation of the energy barriers compared to the pure shear case.

The formation mechanism for the (20 $\bar{1}$)[$\bar{1}0\bar{2}$] type of twin is displayed in Fig. 8(a), viewed from the [0 $\bar{1}0$] direction. The orange crosses denote the motif points in this system. The motif points are defined at the middle of each pair, thus, once a shear is applied, the atoms clustered around the motif point are displaced by the same amount. The inter-planar distance between (20 $\bar{1}$) motif points are measured to be 1.43 Å. Hence, a 0.338 shear generates a displacement of $\bar{b} = 0.48$ that moves the motif units to a twinned position along the (20 $\bar{1}$) boundary. However, additional shuffles of Ni and Ti are required to generate a perfect mirror symmetry. These shuffles are bi-directional in nature (shown in Fig. 8(c)) and locally rearrange the Ni and Ti atoms in [010] and [0 $\bar{1}0$] directions. The magnitude of shuffle was calculated to be 0.32 Å for Ti and 0.32 Å for Ni.

To obtain the PES within reasonable computational time, we divided the shear and shuffle based computational domain primarily into 7 × 7 nodes. Additional nodes are added near the energetically significant positions such as the local minima and the saddle point. A symmetry-adapted “free energy” polynomial was fitted to our $\Delta E(\eta, \varepsilon)$ data. For this fault energy functional $F(\eta, \varepsilon) = \Delta E(\eta, \varepsilon)$, we chose a fourth order cosine-sine polynomial [29], which can appropriately represent the shear shuffle coupling, *i.e.*

$$F(\eta, \varepsilon) = \sum_{m,n=0}^{m+n \leq 4} a_{mn} [X(\eta)]^m [X(\varepsilon)]^n [1 - \delta_{m0} \delta_{n0}] + \sum_{m,n=0}^{m+n \leq 4} b_{mn} [X(\eta)]^m [X(\varepsilon)]^n \quad (1)$$

where, $[X(x)] = [1 - \cos(\pi x)]$, $[Y(x)] = [\sin(\pi x)]$, and δ_{ij} represents Kronecker's delta (δ_{ij} is 1(0) if *i* is (not) equal to *j*). An additional constraint of $|dF/dx|_{x=0,1} = 0$ was imposed to ensure local minima at (0,0) and (1,1) positions in the PES.

The predicted potential energy surface (PES) during 3rd to 4th layer twin formation at zero hydrostatic stress is plotted in Fig. 8(b) (the shear and shuffle directions are normalized). Here we note that, the twin layer growth from the 3rd to 4th layer is specifically chosen, since the effect of mechanical coupling becomes insignificant once the twins grow more than three layer thick and the sinusoidal fault energy pattern is repeated periodically during this twin growth. A mechanical coupling arises from the interaction energy of upper and lower twin boundaries, necessitating 3rd and higher layers for consideration of twin growth behavior. The PES points out that a pure shear ($\varepsilon=0 \rightarrow 1$, $\eta=0$) generates an energetically unstable structure. Similar energy pattern is observed for pure shuffle ($\varepsilon=0$, $\eta=0 \rightarrow 1$) which does not generate a twinned structure. The combination of shear and shuffle ($\varepsilon=1$, $\eta=1$) results in a stable twinned position as manifested by the upper right corner of the PES. Mean energy path (MEP) provides the transition path from this 3rd to 4th layer and is shown by the white line in PES (Fig. 8(b)). The MEP illustrates the complex coupling of shear and shuffle that exist during the twin growth in the (20 $\bar{1}$) plane. Both shear and

Table 1

Summary of the shear magnitudes, the shuffles and the energy barriers associated with different twinning modes in martensitic NiTi.

Twinning plane and direction	Twinning shear	Twinning shuffle (Å)	\bar{b}	Twin energy barrier (mj/m ²)	Unstable slip energy barrier (mj/m ²)
Type II-1 [17]	0.2804	Ni 0.6385 in <205>	1/9[011]	14	620
(001) [100] [18]	0.2385	-	½[100]	7.6	20
(100) [001] [18]	0.2385	Ti 0.46 in [100] Ni 0.23 in [100]	1/13.5[001]	41	448
(20 $\bar{1}$)[$\bar{1}0\bar{2}$]-This study	0.338	Ti 0.32 in [0 $\bar{1}0$] Ni 0.23 in [010]	1/20[$\bar{1}0\bar{2}$]	61	1390

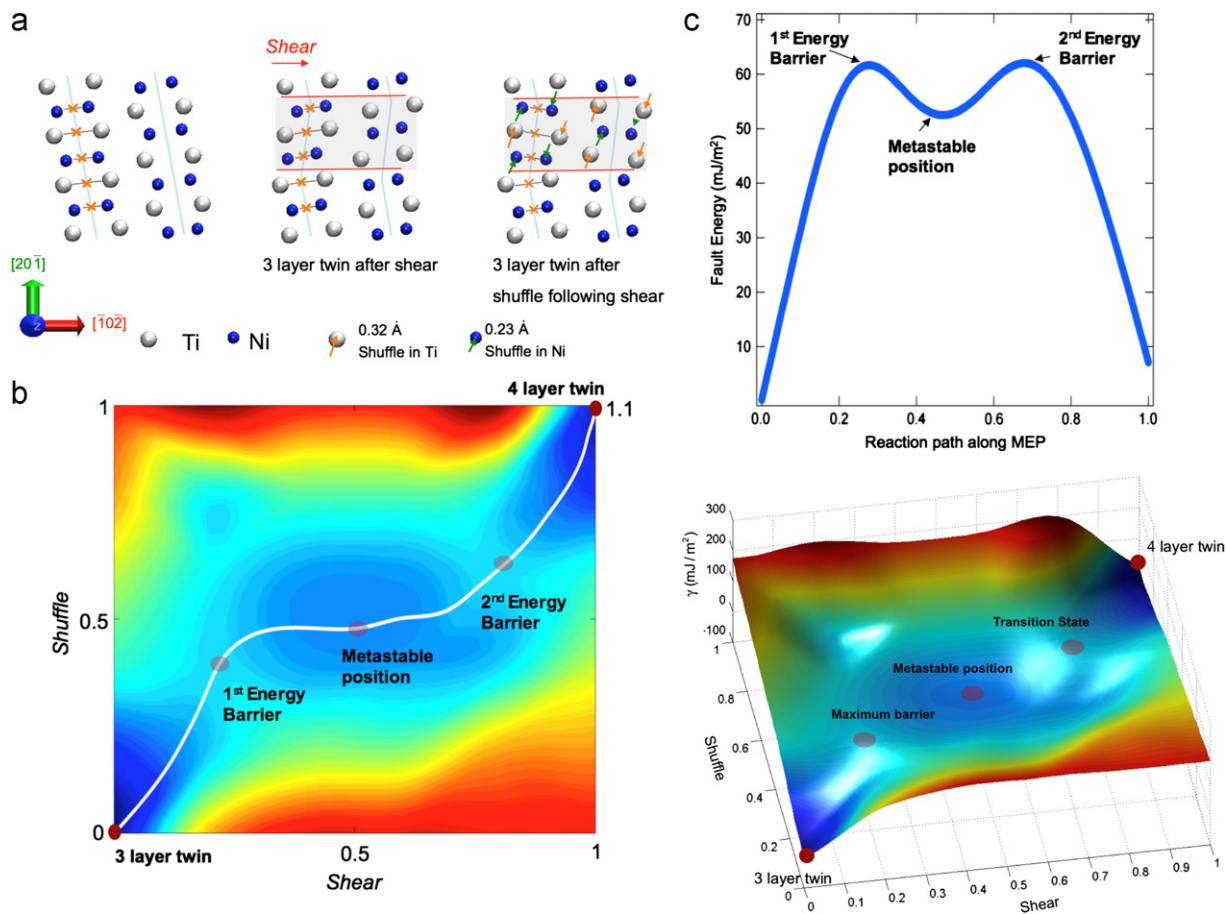


Fig. 8. (a) Shear and shuffles associated with creation of the $(20\bar{1})$ twin (shuffles are shown with arrows) with orange cross showing the motif units; viewing direction is $[0\bar{1}0]$, (b) PES for $(20\bar{1})$ 3rd to 4th layer twin formation, (c) the modified GPFPE along the PES path, (d) an angled view of the energy landscape. (For interpretation of the references to color in this figure legend, the reader is referred to the web version of this article.)

shuffles are operative at the beginning of the twin growth mechanism until a shear of $\varepsilon=0.25$. At this position, the atoms reach the maximum energy barrier which is the transition state (TS). From shear $\varepsilon=0.25$ to $\varepsilon=0.75$, shuffle is insignificant compared to shear. At shear $\varepsilon=0.75$, the atoms reach another peak barrier as shown by the dots in the PES. Shear and shuffle are again operative in the last stage of twin growth mechanism until the stable 4th layer position is reached. The fault energies along the reaction coordinate of the MEP are plotted in Fig. 8(c). The plot shows the two energy peak points along a metastable barrier at $\varepsilon=0.5$, $\eta=0.5$. The magnitudes of the peak points are calculated to be 61 mJ/m^2 . In comparison with the energy barrier during the (001) and (100) twin growth, this is of a higher magnitude.

3.2. GSFE- $(20\bar{1})[\bar{1}0\bar{2}]$

The atomic arrangement of atoms for the GSFE path for the $(20\bar{1})[\bar{1}0\bar{2}]$ system is given in Fig. 9(a) and (b). As discussed earlier, GSFE provides the maximum energy barrier the atoms have to overcome during their glide in a certain plane and direction. In addition to that, GSFE provides vital information about the magnitude of Burgers vector of a possible dislocation in that system with a metastable position. Fig. 9(c) provides the energy barrier associated with slip, and points out a metastable position at $\frac{1}{2}[\bar{1}0\bar{2}]$. However, to reach this metastable position, the atoms have to overcome a barrier energy of 1390 mJ/m^2 . This energy is appreciably high compared to slip barriers in martensite in the $(001)[100]$ system. Theoretical shear stress for slip nucleation can be estimated from the slope of the GSFE curve as follows, $(\tau_{SLIP})_{ideal} = \delta\gamma/\delta u_x|_{max}$.

This value is calculated and found to be 107 GPa. This magnitude of stress is excessively high for a full dislocation to glide in this system and points out to the energetic basis for the absence of full or partial dislocation in this plane. The absence of twinning partially signifies that any twin formation or growth in the $(20\bar{1})[\bar{1}0\bar{2}]$ system will be in conjunction with a shear and shuffle as noted earlier.

4. Summary of results

Mechanical twinning is a significant deformation mechanism in NiTi martensites. In this study, we focused on the characterization of the $(20\bar{1})$ system which is important for modeling the constitutive response of shape memory alloys as well as in extending the ductility to larger strains.

We make a clear distinction between the energies required for twin growth versus slip transmission. The twinning stress depends on the fault energies of the Type II-1, (001) and (100) systems which are activated at early stages of the deformation. At later stages of the deformation, the $(20\bar{1})$ system develops which interacts with the existing twin systems. Through atomic simulations, it was possible to determine the complex shear and shuffle path that generates the $(20\bar{1})$ twin in martensitic NiTi. The results show that the twinning in this system is favored over slip. This is shown precisely by determining the Generalized Stacking Fault Energy (GSFE) and Generalized Planar Fault Energy (GPFPE) curves for twin versus slip modes. High stress levels, either applied externally or those that develop intrinsically via precipitates and defects can readily contribute to the activation of this

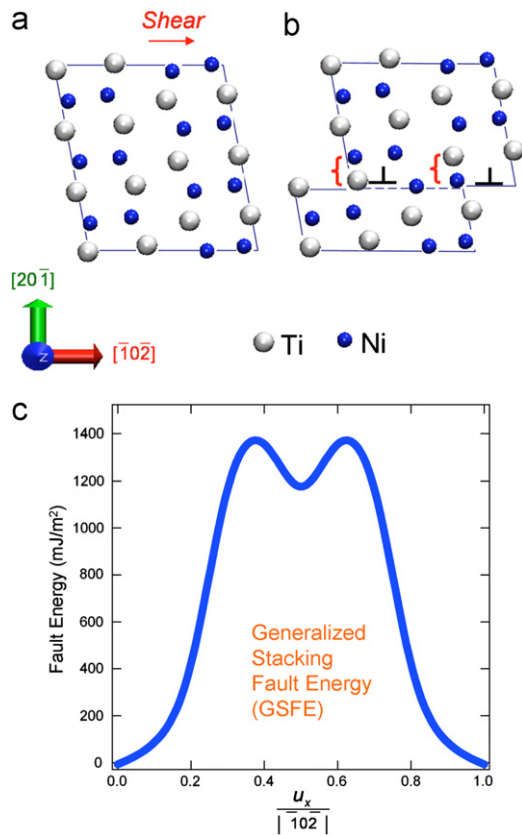


Fig. 9. (a) Shears associated with slip for the $(20\bar{1})$ twin, (b) atomic position of possible dislocation glide in the $(20\bar{1})[\bar{1}02]$ system. The red curly parenthesis point to the short near neighbor distance once the atoms are moved a displacement of $u_x/|\bar{1}02|=0.5$, (b) the GSFE curve associated with slip displaying substantially high barriers. (For interpretation of the references to color in this figure legend, the reader is referred to the web version of this article.)

system. We illustrated with energetic barrier calculations that twin migration is preferred in contrast to dislocation motion. The role of shuffles is to create a considerable divergence between the GSFE and GPFE behaviors. We note that at very high stresses dislocations can nucleate and glide and this could cause irreversibilities in shape memory response.

The use of digital image correlation proved to be valuable in confirming the twinning-induced strains associated with the (001) , (100) and $(20\bar{1})$ systems. These twins intersect and result in additional hardening of the NiTi martensite. This is clear from the experimental results where the slope exhibits an upward curvature. This hardening behavior combined with the additional ductility attributed to the $(20\bar{1})$ extends the utility of NiTi shape memory alloy. Because the twins are extremely fine and are of nanodimensions, digital image correlation maps the associated strain fields at the mesoscale. Thus, considerable insight is only gained by utilizing DIC in conjunction with microscopy and atomic simulations.

We note that $(20\bar{1})$ boundary falls into the sigma 3 category, and its visualization is complex. Considering the monoclinic crystallography, special codes are written to visualize the planes and shear directions. Particularly, we note that the shuffles are not in plane with the shear. This is rather different than the cubic (001) and (100) systems where the planes can be visualized more readily. The twinning shear magnitude for the $(20\bar{1})$ reported in this study can thus be calculated. As noted earlier, the $(20\bar{1})$ permits a higher twinning shear compared to the (001) and (100) cases. The critical shear stresses (ideal case) for twinning were calculated based on the unstable and twin fault energies as $\tau_{TMideal} = \pi\{\gamma_{TM}/\bar{b}_{twin}\}$ where $\gamma_{TM} = \gamma_{ut} - 2\gamma_{tsf}$ is referred to as the

twin migration energy (Table 2). On the other hand, theoretical slip nucleation was estimated from the slope of the GSFE curve as before, $(\tau_{SLIP})_{ideal} = \delta\gamma/\delta u_x|_{max}$, (Table 3). More sophisticated versions have been proposed in incorporating the elastic energies associated with the twin nucleus [30].

We note that the shear magnitudes for the (001) , (100) and $(20\bar{1})$ cases are smaller (see Table 1) than those observed in fcc and bcc lattices (0.707), hence, elastic accommodation of such twins is more likely increasing the reversibility of transformation in the case of NiTi.

A combined shear and shuffle mechanism is presented that facilitates the formation of twins. Clearly, based on the atomic simulation results, the slip resistance in the $\{201\}$ system is very high ruling out the likelihood of plastic flow due to slip. Shuffles permit reflective symmetry across the coherent twin boundaries, and shuffles lower the energy barrier. This is different than the classical description of twinning which relies on a shearing mechanism via glide of partial dislocations only. The combined shear shuffle induced twinning opens new venues for design of shape memory alloys where flow due to slip will be curtailed. Here we note that, while first principle based *ab-initio* calculations are highly suitable to point out the exact mechanism of twin formations and a highly accurate energetic barrier during twin and slip mechanisms, it is unable to shed light on the contributions of cold deformation, grain refinement or precipitation due to the current computational time limitation. To account for such complex hardening processes in a physics based model, a rigorous multi-scale method at different length scales is required that combines continuum and atomistic calculations.

We finally point to an important implication of the results. When the martensite reverts to austenite a fraction of the $(20\bar{1})$ and (113) twins transform to an austenitic twinned structure [24,31]. Upon transformation the conjugate twins in austenite are

Table 2

Twin migration stress for different twin modes in NiTi martensite.

K_1	η_1	$(\tau_{TMideal} = \pi\{\gamma_{TM}/\bar{b}_{twin}\})$ (GPa)
(001)	$[100]$	0.165
(100)	$[001]$	1.79
$(20\bar{1})$	$[\bar{1}02]$	3.9

Table 3

Slip nucleation stress in NiTi martensite

K_1	η_1	$(\tau_{shear})_{ideal} = \frac{\delta\gamma}{\delta u_x} _{max}$ (GPa)
(001)	$[100]$	0.277
(100)	$[001]$	4.5
$(20\bar{1})$	$[\bar{1}02]$	107

Table A1

Resolution at several magnifications. The number of images refers to the number of overlapping images required to cover the region of interest at that specific magnification. The last column (column 4) is the subset size in pixels, the number shown in parenthesis is the subset size in microns which is calculated by multiplying the subset size by the resolution (column 3).

Magnification	Images captured	Number of images	Resolution ($\mu\text{m}/\text{pix}$)	Subset size in pixels (μm)
$1.6 \times$	<i>In-situ</i>	1	2.876	51 (146.7)
$5 \times$	<i>Ex-situ</i>	6	0.868	51 (44.3)
$10 \times$	<i>Ex-situ</i>	28	0.436	51 (22.2)
$25 \times$	<i>Ex-situ</i>	35	0.174	51 (8.9)
$50 \times$	<i>Ex-situ</i>	35	0.087	101 (8.8)

observed specified as (114) and (112). If domains of slip are limited [32], this could increase the potential for higher transformation strains in NiTi shape memory.

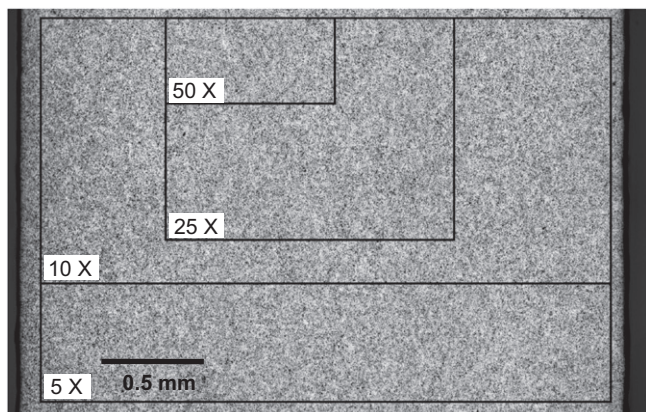


Fig. A1. Regions imaged at four different magnifications. Arrays of high resolution images of the reference and deformed region were captured in the optical microscope (see Table A1 for number of images at each magnification). Note that the regions overlap.

Acknowledgments

The work was supported by the NSF Grant CMMI-09-26813 and partly by DMR-08-03270. The authors acknowledge Dr. S. Dilibal with assistance in the experiments.

Appendix

High resolution, *ex-situ* DIC measurements were performed after loading a NiTi sample in the martensitic phase. Residual strain measurements were obtained at different points. The images of reference and deformed states were captured with the optical microscope at four different magnifications (zero load). The sample had to be removed from the load frame each time microscope images were captured.

The DIC resolution, which can be approximated by subset size, is dependent on the magnification level at which images are taken. Higher magnification leads to improved resolution. Table A1 lists the different magnifications used in this experiment along with the corresponding image resolution. This in conjunction with the quality of the speckle pattern determines the final subset size that can be used for the correlation. Smaller subset sizes improve the

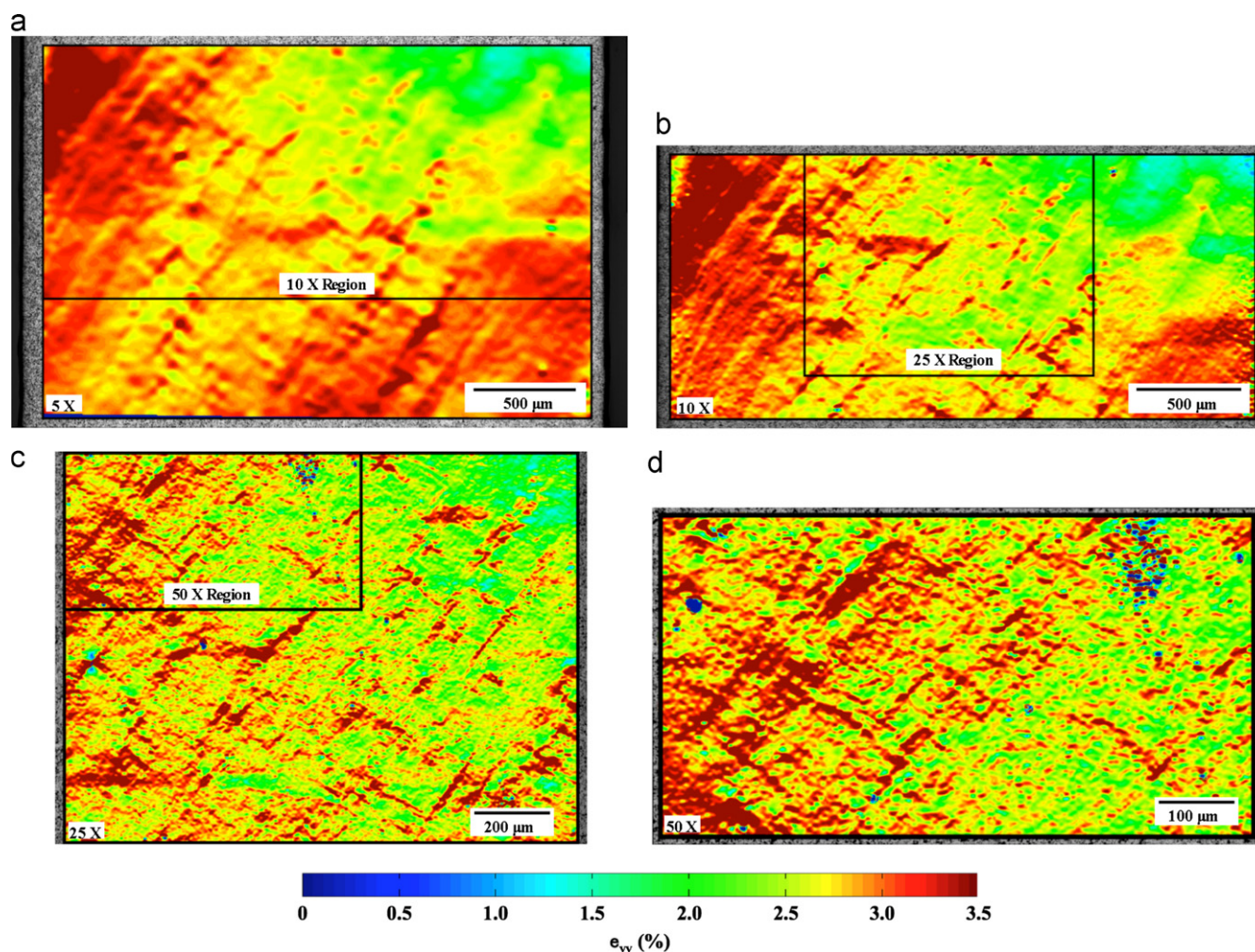


Fig. A2. *Ex-situ* DIC contour plots (a) Contour plot of the e_{yy} strain field with DIC images captured at $5\times$ magnification. The area outlined with the white rectangle delineates the region of interest at $10\times$ magnification. (b) Contour plot of the e_{yy} strain field with DIC images captured at $10\times$ magnification. The area outlined with the blue rectangle delineates the region of interest at $25\times$ magnification. (c) Contour plot of the e_{yy} strain field with DIC images captured at $25\times$ magnification. The area outlined with the black rectangle delineates the region of interest at $50\times$ magnification. (d) Contour plot of the e_{yy} strain field with DIC images captured at $50\times$ magnification. Note the improvement in strain field resolution as the magnification is increased. (For interpretation of the references to color in this figure legend, the reader is referred to the web version of this article.)

spatial resolution of the DIC fields. This is accomplished by reducing the amount of strain averaging, typically performed in correlations with larger subset sizes.

The downside of increasing magnification is the reduction of field of view (*i.e.*, reduction in image size) [25]. Thus, the area that can be monitored with one image will become small which in turn requires multiple images to be captured to cover the required region of interest. With reference and deformed image arrays acquired, there are two options available to obtain the strain fields throughout the region of interest resulting from the applied deformation: (1) the image arrays can be stitched together to cover large domains on which DIC can be performed; or (2) each pair of reference and deformed images can be correlated individually, and the DIC strain fields resulting from all of the correlations can then be stitched together. The problem with the first method is that it introduces some errors in the strain fields due to image stitching. The relative error decreases as the total strain in the area of interest increases. Carroll et al. [33] have demonstrated this method for a polycrystalline material and have reported a maximum error of 0.25% in the measured strain fields. The second method does not have stitching errors, but the procedure of obtaining the strain fields through individual image correlation is significantly more time consuming compared to the first method [33]. In the results reported here, the first stitching method was selected since relatively high residual strains are considered.

The regions of interest for the four different magnifications are shown in Fig. A1. Each rectangle shows the total sample surface imaged at that magnification. The number of images that were captured to cover the marked regions is listed in Table A1. All the areas overlap, but the size of the region was reduced as the magnification was increased. This was done to keep the number of images reasonable. Since the optical microscope was used in acquiring the *ex-situ* images, it was difficult to mark these regions in the *in-situ* images (captured using conventional camera/lens system). The dissimilar lighting conditions and the large difference in resolution are the main factors that prevent such a relation to be established.

A clear localized response with *bands* of strain accumulation was observed (Fig. 7). At least three strain bands can be identified. A high level of heterogeneity can be seen in the contour plots shown in Fig. A2. Some regions show pronounced activity while other regions have significantly lower level of strain accumulation.

The improvement in strain field resolution, as magnification is increased; helps to delineate the features of the strain field better (*i.e.* bands become sharper and more pronounced). This provides better chances to correlate these features with twinning in the material.

References

- [1] K. Otsuka, C.M. Wayman, Cambridge University Press, Cambridge, 1998.
- [2] Y. Liu, Z. Xie, J. van Humbeeck, L. Delaey, L. Yinong, *Philos. Mag. A* 80 (2000) 1935.
- [3] S. Miyazaki, K. Otsuka, Y. Suzuki, *Scr. Metall.* 15 (1981) 287–292.
- [4] T. Saburi, S. Nenno, in: H.I. Aaronson, D.E. Laughlin, R.F. Sekerka, C.M. Wayman (Eds.), *International Conference on Solid-Solid Phase Transformations*, Pittsburgh, 1981, pp. 1455–1479.
- [5] M. Nishida, C.M. Wayman, A. Chiba, *Metallography* 21 (1988) 275–291.
- [6] M. Nishida, H. Ohgi, I. Itai, A. Chiba, K. Yamauchi, *Acta Metall. Mater.* 43 (1995) 1219–1227.
- [7] J.X. Zhang, M. Sato, A. Ishida, *Acta Mater.* 54 (2006) 1185.
- [8] N.S. Surikova, Y.I. Chumlyakov, *Phys. Metals Metallogr.* 89 (2000) 196.
- [9] K. Gall, H. Sehitoglu, *Int. J. Plasticity* 15 (1999) 69.
- [10] C. Nielaeyts, T. Ben Zineb, S. Arbab-Chirani, E. Patoor, *Int. J. Plasticity* 18 (2002) 1619.
- [11] K. Gall, T.J. Lim, D.L. McDowell, H. Sehitoglu, Y.I. Chumlyakov, *Int. J. Plasticity* 16 (2000) 1189–1214.
- [12] F. Patoor, M. El Amrani, A. Eberhardt, M. Berveiller, *J. Phys.* 5 (1995) 2.
- [13] Z. Bo, D.C. Lagoudas, *Int. J. Eng. Sci.* 37 (1999) 1089.
- [14] M. Huang, L.C. Brinson, *J. Mech. Phys. Solids* 46 (1998) 1379.
- [15] S. Kibey, H. Sehitoglu, D.D. Johnson, *Acta Mater.* 57 (2009) 1624.
- [16] H. Xiangyang, G.J. Ackland, K.M. Rabe, *Nat. Mater.* 2 (2003) 307.
- [17] T. Ezaz, H. Sehitoglu, *Appl. Phys. Lett.* 98 (2011) 141906.
- [18] T. Ezaz, H. Sehitoglu, *Acta Mater.* (2011).
- [19] D. Farkas, D. Roqueta, A. Vilette, K. Ternes, *Modelling Simulation Mater. Sci. Eng.* 4 (1996) 359–369.
- [20] W.S. Lai, B.X. Liu, *J. Phys.: Condens. Matter* 12 (2000) 53–60.
- [21] T. Ezaz, H. Sehitoglu, *Appl. Phys. Lett.* 98 (2011) 241906.
- [22] M. Krishnan, J.B. Singh, *Acta Mater.* 48 (2000) 1325.
- [23] T. Onda, Y. Bando, T. Ohba, K. Otsuka, *Mater. Trans. JIM* 33 (1992) 354.
- [24] I. Karaman, A.V. Kulkarni, Z.P. Luo, *Philos. Mag.* 85 (2005) 1729.
- [25] C. Efstathiou, H. Sehitoglu, J. Lambros, *Int. J. Plasticity* 26 (2010) 93.
- [26] G. Kresse, J. Hafner, *Phys. Rev. B* 48 (1993) 13115.
- [27] J.P. Perdew, K. Burke, M. Ernzerhof, *Phys. Rev. Lett.* 77 (1996) 3865.
- [28] L. Maragliano, A. Fischer, E. Vanden-Eijnden, G. Ciccotti, *J. Chem. Phys.* 125 (2006) 24106.
- [29] J.B. Liu, D.D. Johnson, *Phys. Rev. B* 79 (2009) 134113.
- [30] S. Kibey, J.B. Liu, D.D. Johnson, H. Sehitoglu, *Acta Mater.* 55 (2007) 6843.
- [31] M. Nishida, S. Ii, K. Kitamura, T. Furukawa, A. Chiba, T. Hara, K. Hiraga, *Scr. Mater.* 39 (1998) 1749.
- [32] Y. Liu, G. Tan, S. Miyazaki, *Mater. Sci. Eng. A* 438–440 (2006) 612–616.
- [33] J. Carroll, W. Abuzaid, J. Lambros, H. Sehitoglu, *Rev. Sci. Instrum.* 81 (2010) 083703. (083709 pp.).